

# Quantum Tomography of Suspended Carbon Nanotubes

Jialiang Chang, Nicholas Pietrzak, and Cristian Staii\*

Department of Physics and Astronomy, Tufts University, Medford, MA, 02155, USA

(Dated: September 3, 2025)

We present an all-mechanical protocol for coherent control and full quantum-state reconstruction of the fundamental flexural mode of a suspended carbon nanotube (CNT). Calibrated impulses from a nearby atomic force microscope (AFM) tip serve a dual role: they implement mechanical  $\pi/2$  rotations for Ramsey interferometry and realize phase-space displacements for Wigner function tomography via displaced-parity sampling. The same actuator thus unifies control and tomography while avoiding optical heating and eliminating on-chip microwave drive lines at the resonator. We derive explicit control pulse sequences and a master-equation description that map measured signals onto the energy-relaxation and phase-coherence times, as well as onto parity-based quantum signatures, including negative regions of the Wigner function. The approach is compatible with multiple readout modalities: direct AFM deflection, dispersive coupling to a Cooper-pair box, and dispersive microwave cavity probing. Together, these techniques provide complete access to populations, coherence, and parity within a single device architecture. This minimal scheme provides a practical route to all-mechanical quantum control and state-resolved characterization of decoherence in mesoscopic mechanical systems.

*Introduction* – Probing quantum decoherence in mesoscopic mechanical systems is a fundamental challenge in the pursuit of quantum technologies and tests of macroscopic quantum phenomena [1–4]. Nanomechanical oscillators are a natural testbed for such investigations due to their high sensitivity to environmental interactions and potential for nonclassical behavior [5–9]. Within these platforms, suspended carbon nanotubes (CNTs) are among the lightest high- $Q$  mechanical resonators, exhibiting zero-point motion amplitudes  $x_{\text{zpf}}$  in the picometer range and large frequency-to-mass ratios [10–13]. Their small dimensions and strong coupling to external forces enable precise manipulation and detection of vibrational states, making them well suited for probing quantum decoherence mechanisms in mechanical systems [14–17]. Bringing such resonators into the regime of coherent control enables tests of macroscopic quantum behavior and opens opportunities for ultrasensitive force and field sensing. However, despite advances in cooling and dispersive sensing, a compact, experimentally simple route to both coherent control and full quantum-state reconstruction of a CNT mechanical mode has remained difficult to achieve.

In this Letter, we propose and analyze an all-mechanical protocol that achieves coherent control and tomography of a single suspended CNT. Short, calibrated impulses from a nearby atomic force microscope (AFM) tip serve a dual role: they implement mechanical  $\pi/2$  rotations for Ramsey interferometry and realize phase-space displacements for the reconstruction of the Wigner function via displaced-parity sampling. This purely mechanical actuation avoids optical heating and eliminates on-chip microwave drive lines at the resonator, while retaining nanometer-scale spatial selectivity and sub-femtonewton scale force resolution. The readout is compatible with three complementary transducers: direct AFM deflection, dispersive coupling to a Cooper-pair

box (CPB), and dispersive microwave cavity probing, allowing single-mode populations, coherence, and parity to be measured within the same device architecture.

The novelty of our approach is in the integration of Ramsey interferometry and Wigner tomography for a mesoscopic CNT mechanical resonator using a single, precisely controlled actuator. This unified, all-mechanical scheme provides a minimal, experimentally implementable toolbox for preparing, manipulating, and characterizing quantum states of motion. By linking the Ramsey fringe envelope to the phase-coherence time  $T_2$  and the ringdown to the energy-relaxation time  $T_1$ , and by extracting displaced-parity maps directly from measured populations, the protocol provides a quantitative, state-resolved measure of decoherence and quantum behavior, including negative regions of the Wigner function, in a minimal and scalable experimental platform. Establishing coherent control and tomography in CNT resonators opens a new route to precision tests of macroscopic quantum phenomena and to ultrasensitive sensing modalities that harness quantum resources in nanomechanics.

*Model* – At dilution-refrigerator temperatures ( $T = 50$  mK), in ultrahigh vacuum ( $P < 10^{-7}$  Torr), and after sideband or feedback cooling to a mean phonon occupancy  $\bar{n} \ll 1$ , the CNT motion is effectively confined to its ground and first-excited flexural states  $\{|0\rangle, |1\rangle\}$  [3, 6, 18, 19]. We represent this subspace with Pauli operators  $\sigma_z = |1\rangle\langle 1| - |0\rangle\langle 0|$  and  $\sigma_x = |0\rangle\langle 1| + |1\rangle\langle 0|$ . A nearby AFM tip applies a controllable, near-resonant force  $F(t) = F_0 \cos(\omega_d t)$  on the CNT displacement (Fig. 1), yielding the laboratory-frame Hamiltonian

$$H_{\text{lab}} = \frac{\hbar\omega_0}{2} \sigma_z + \hbar g \cos(\omega_d t) \sigma_x, \quad (1)$$

where  $\hbar\omega_0$  is the level splitting, and  $g \equiv F_0 x_{\text{zpf}}/\hbar$  is the drive strength set by the AFM force and the zero-point

amplitude  $x_{\text{zpf}}$ . Moving to a frame rotating at  $\omega_d$  and invoking the rotating-wave approximation (RWA) gives [20]:

$$H_S = \frac{\hbar\Delta}{2} \sigma_z + \frac{\hbar\Omega_R}{2} \sigma_x, \quad (2)$$

with detuning  $\Delta \equiv \omega_0 - \omega_d$  and on-resonance Rabi frequency  $\Omega_R = F_0 x_{\text{zpf}}/\hbar$ .

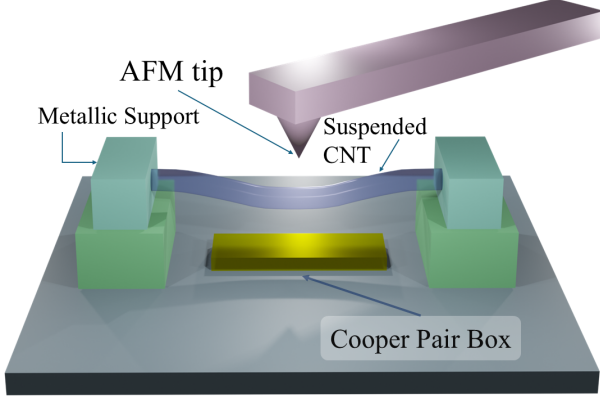


FIG. 1. Schematics of the proposed experimental setup. A doubly clamped single-walled carbon nanotube (CNT) of length  $L = 100\text{--}1000\text{ nm}$  is suspended over a  $200\text{ nm}$  trench and coherently driven by sub-femtonewton forces from a nearby atomic force microscope (AFM) tip. This experimental configuration provides a fully mechanical platform for implementing Ramsey interferometry and Wigner-function tomography of a nanomechanical mode under dilution-refrigerator conditions ( $T = 50\text{ mK}$ ,  $P < 10^{-7}\text{ Torr}$ ). Also indicated schematically is a Cooper-pair box patterned on the  $\text{SiO}_2/\text{Si}$  substrate, illustrating one possible dispersive-coupling readout scheme for the CNT.

Coupling the CNT to a cryogenic bosonic environment induces dissipation and dephasing, described by a GKSL master equation for the reduced density matrix  $\rho_S$  [20]:

$$\dot{\rho}_S = -\frac{i}{\hbar}[H_S, \rho_S] + \gamma_{\downarrow} \mathcal{D}[\sigma_-]\rho_S + \gamma_{\uparrow} \mathcal{D}[\sigma_+]\rho_S + \gamma_{\varphi} \mathcal{D}[\sigma_z]\rho_S, \quad (3)$$

with  $\sigma_+ = |1\rangle\langle 0|$ ,  $\sigma_- = |0\rangle\langle 1|$ , and the dissipator  $\mathcal{D}[\sigma]\rho_S = \sigma\rho_S\sigma^\dagger - \frac{1}{2}\{\sigma^\dagger\sigma, \rho_S\}$ . Here  $\gamma_{\downarrow}$  ( $\gamma_{\uparrow}$ ) is the relaxation (thermal excitation) rate set by the bath spectral density at  $\omega_0$ , and  $\gamma_{\varphi}$  accounts for pure dephasing, typically dominated by low-frequency phase noise. The corresponding time constants

$$T_1 \equiv \frac{1}{\Gamma_1}, \quad T_2 \equiv \frac{1}{\Gamma_2}, \quad \Gamma_1 \equiv \gamma_{\downarrow} + \gamma_{\uparrow}, \quad \Gamma_2 \equiv \frac{\Gamma_1}{2} + \gamma_{\varphi}, \quad (4)$$

quantify longitudinal energy relaxation ( $T_1$ ) and transverse phase coherence ( $T_2$ ) [9, 21].

Writing  $\rho_S = \frac{1}{2}(\mathbb{1} + X\sigma_x + Y\sigma_y + Z\sigma_z)$  yields the Bloch

equations [20]:

$$\dot{X} = -\Gamma_2 X + \Delta Y, \quad (5)$$

$$\dot{Y} = -\Gamma_2 Y - \Delta X + \Omega_R Z, \quad (6)$$

$$\dot{Z} = -\Gamma_1(Z - Z_{\text{eq}}) - \Omega_R Y, \quad (7)$$

with  $Z_{\text{eq}} = (\gamma_{\uparrow} - \gamma_{\downarrow})/\Gamma_1 \approx -1$  for an Ohmic spectral density at dilution temperatures [21]. The excited-state population is  $P_1 = (1 + Z)/2$ . Eqs. (4)–(7) clarify the relevant control and decay scales: the oscillator frequency  $\omega_0$  defines the intrinsic timescale, the Rabi frequency  $\Omega_R$  controls the coherent rotation rate induced by AFM driving, and the detuning  $\Delta$  determines the Bloch vector precession during free evolution (Ramsey phase accumulation). The transverse coherence time  $T_2$  fixes the fringe contrast, while the longitudinal relaxation time  $T_1$  governs the free decay of the population (“ringdown”) once the drive is switched off. Under continuous resonant drive, the steady state reflects competition between the drive strength and two relaxation channels: energy exchange with the bath ( $T_1$ ) and loss of phase coherence ( $T_2$ ). Operationally,  $T_1$  sets the rate of energy dissipation/repopulation, whereas  $T_2$  determines how long the relative phase between  $|0\rangle$  and  $|1\rangle$  is maintained, thereby controlling the visibility of Ramsey fringes and limiting the spectroscopic linewidth.

*Rabi Oscillations* – On resonance ( $\Delta = 0$ ), at dilution temperatures, and with the system initialized in  $|0\rangle$ , the driven CNT qubit undergoes damped Rabi oscillations. Solving the Bloch equations (5)–(7) and defining the underdamped frequency  $\Omega_d = \sqrt{\Omega_R^2 - (\Gamma_1 - \Gamma_2)^2/4}$ , we obtain the excited-state occupation probability in the compact form [20]:

$$P_1(t) = P_1^{(\infty)} \left[ 1 - e^{-(\Gamma_1 + \Gamma_2)t/2} \left( \cos(\Omega_d t) + \frac{\Gamma_1 - \Gamma_2}{2\Omega_d} \sin(\Omega_d t) \right) \right], \quad (8)$$

with the on-resonance steady state

$$P_1^{(\infty)} = \frac{\Omega_R^2}{2(\Omega_R^2 + \Gamma_1\Gamma_2)}. \quad (9)$$

In the relaxation-limited regime with negligible pure dephasing ( $\gamma_{\varphi} \approx 0$ ), one has  $\Gamma_2 \approx \Gamma_1/2$ , and the Rabi oscillation envelope decays at rate  $3\Gamma_1/4$ . Additional pure dephasing increases  $\Gamma_2$  while leaving  $\Gamma_1$  unchanged, thereby reducing the oscillation visibility and shrinking the underdamped window  $\Omega_R > \frac{1}{2}|\Gamma_1 - \Gamma_2|$ . The free population ringdown time remains set by  $T_1$ . Fig. 2(a) displays the time evolution of the excited-state occupation probability for different values of the oscillation parameters.

*Ramsey Interferometry* – This technique provides a phase-sensitive probe of coherence complementary to the driven dynamics of Rabi oscillations. In the present scheme a calibrated AFM tip generates two *mechanical*

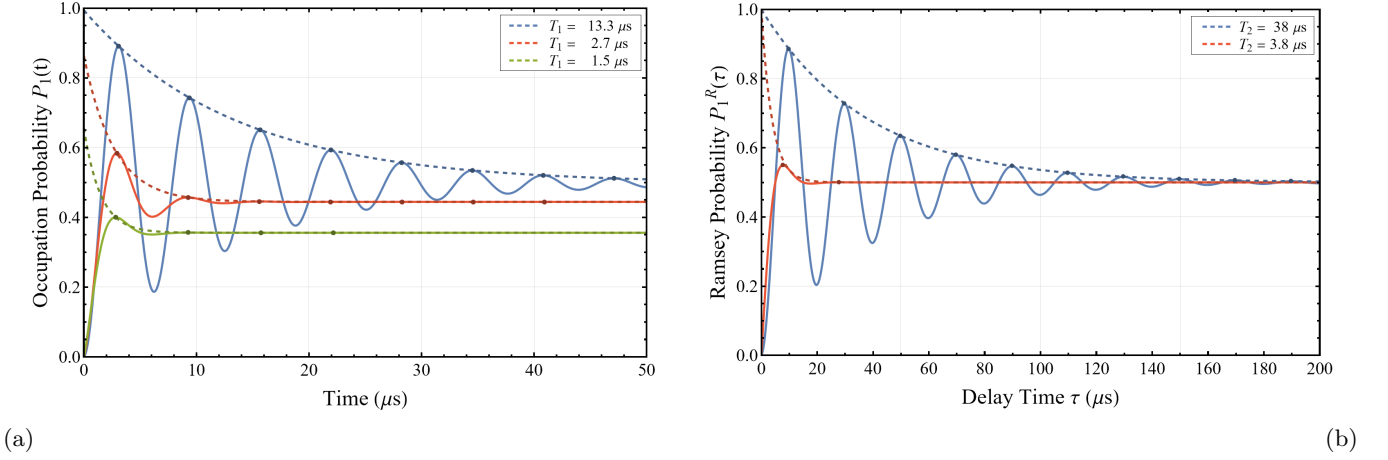


FIG. 2. (a) Excited-state population  $P_1(t)$  of a driven CNT in three damping regimes: strong driving ( $\Gamma_1/\Omega_R = 0.1$ , blue), underdamped ( $\Gamma_1/\Omega_R = 0.5$ , red), and near-critical ( $\Gamma_1/\Omega_R = 0.9$ , green). The Rabi frequency is  $\Omega_R = 0.75 \text{ MHz}$  for all curves. Dotted lines are fits to Eq. (8) used to extract  $T_1$ . (b) Ramsey population  $P_1^R(\tau)$  versus delay for detuning  $\Delta = 300 \text{ kHz}$  in two CNT devices of different lengths:  $L = 800 \text{ nm}$  (blue) and  $L = 250 \text{ nm}$  (red). Dotted lines are fits to Eq. (10) used to extract  $T_2$ .

$\pi/2$  pulses separated by a free-evolution interval  $\tau$ . The pulse sequence is:

$$|0\rangle \xrightarrow{\pi/2} \frac{|0\rangle + |1\rangle}{\sqrt{2}} \xrightarrow{\text{free } \tau} \rho(\tau) \xrightarrow{\pi/2} \rho_{\text{out}}(\tau) \xrightarrow{\text{readout}} P_1^R(\tau).$$

The first pulse creates a  $\pi/2$  rotation for a short resonant drive  $t_{\pi/2} = \pi/(2\Omega_R)$ , and prepares the CNT qubit in a coherent superposition  $|\psi(0)\rangle = (|0\rangle + |1\rangle)/\sqrt{2}$ . During the subsequent delay interval  $\tau$  the Bloch vector precesses at the detuning frequency  $\Delta$ , and the system acquires a relative phase  $\Delta\tau$  induced by the unitary evolution. The second  $\pi/2$  pulse converts the accumulated phase into a population difference, yielding the excited-state probability [20]:

$$P_1^R(\tau) = \frac{1}{2} \left[ 1 + e^{-\tau/T_2} \cos(\Delta\tau + \phi_0) \right], \quad (10)$$

where  $\phi_0$  captures any programmed phase shift between AFM pulses. Immediately after the second pulse,  $P_1^R(\tau)$  is measured using any of the compatible transducers described below (AFM deflection, dispersive Cooper-pair box, or cavity reflectometry). Sweeping  $\tau$  produces Ramsey fringes whose frequency is set by the detuning  $\Delta$  and whose envelope decays with  $T_2$ . We operate with  $\Omega_R, \Delta \ll \omega_0$  (RWA regime) and use short pulses,  $t_{\pi/2} \ll \tau, T_2$ , so decoherence during the pulses is negligible. The relative phase  $\phi_0$  is set by timing the second pulse with respect to the drive. On resonance ( $\Delta = 0$ ) this enables phase scans at fixed  $\tau$ . Projective measurements in the  $\{|0\rangle, |1\rangle\}$  basis then return  $P_1^R(\tau)$  with explicit dependence on the accumulated phase  $\Delta\tau$  or the programmed phase  $\phi_0$  (Eq. (10)). Fig. 2(b) shows the plot of the Ramsey probability as a function of the delay time for different drive and dephasing parameters. The  $\tau$ -dependent

modulation of the measurement statistics provides direct evidence of a coherent superposition of the two levels. The energy-relaxation time  $T_1$  can be obtained independently from the ringdown,  $T_1 = Q/\omega_0$ , where  $Q$  is the CNT mechanical quality factor [14]. This all-mechanical implementation eliminates on-chip microwave drive lines at the resonator, avoids optical heating, and uses the same actuator to deliver phase-space displacements for Wigner tomography, thereby unifying control and state reconstruction in a single device.

*Wigner tomography* – The Wigner function  $W(\alpha)$  provides a complete quasi-probability description of the CNT flexural mode in phase space [8, 17, 22–26]. In this scheme, a short near-resonant AFM impulse implements the phase-space displacement

$$D(\alpha) = \exp(\alpha a^\dagger - \alpha^* a), \quad \alpha = \frac{F_0 t_d}{\sqrt{2m_{\text{eff}} \hbar \omega_0}} e^{i\phi_d}, \quad (11)$$

where  $F_0$  and  $t_d$  are the pulse amplitude and duration,  $\phi_d$  is the phase of the AFM drive relative to the oscillator, and  $m_{\text{eff}}, \omega_0$  are the effective mass and fundamental frequency of the CNT fundamental flexural mode. After the calibrated displacement, measuring the parity operator  $\hat{\Pi} = e^{i\pi a^\dagger a} = (-1)^{\hat{n}}$  yields the displaced-parity form of the Wigner function [22–24]:

$$W(\alpha) = \frac{2}{\pi} \text{Tr}[D(-\alpha) \rho_S D(\alpha) \hat{\Pi}] \quad . \quad (12)$$

Thus, the same AFM actuator that generates  $\pi/2$  rotations (Rabi/Ramsey calibration) also provides the controlled phase-space displacements required for Wigner tomography. Parity is converted to a measured excited state population by a Ramsey-type sequence  $\{\pi/2, t_\pi, -\pi/2\}$  that accumulates a number-dependent phase  $\chi \hat{n} t_\pi$ . Choosing  $t_\pi = \pi/\chi$  implements the parity

phase  $e^{i\pi\hat{n}}$ . Here  $\chi$  is the effective parity-mapping rate per phonon set by the CPB-CNT or cavity-CNT dispersive coupling (details in [Appendices A, B, C](#)). This yields the excited-state probability [22–24]:

$$P_1(\alpha) = \frac{1}{2} \left[ 1 - \frac{\pi}{2} W(\alpha) \right], \quad 2\pi/\omega_0 \ll t_\pi \ll T_2. \quad (13)$$

Sweeping  $\alpha$  on a grid maps  $W(\alpha)$  directly via displaced-parity measurements, without any inverse transform or numerical reconstruction. The contrast across the map is limited by  $T_2$  during the parity mapping window  $t_\pi$  and by any displacement-induced dephasing. Fig. 3 shows the time evolution of the calculated  $W(\alpha)$  for the CNT [20]. Regions with  $W(\alpha) < 0$  are a hallmark of non-classicality, reflecting quantum interference of coherently superposed vibrational states (Figs. 3(a) and 3(b)). As the CNT mode evolves under environmental decoherence (energy relaxation and dephasing), these interference features are progressively washed out, and  $W(\alpha)$  approaches the positive, broadened thermal Wigner distribution of the steady state (Figs. 3(c) and 3(d)).

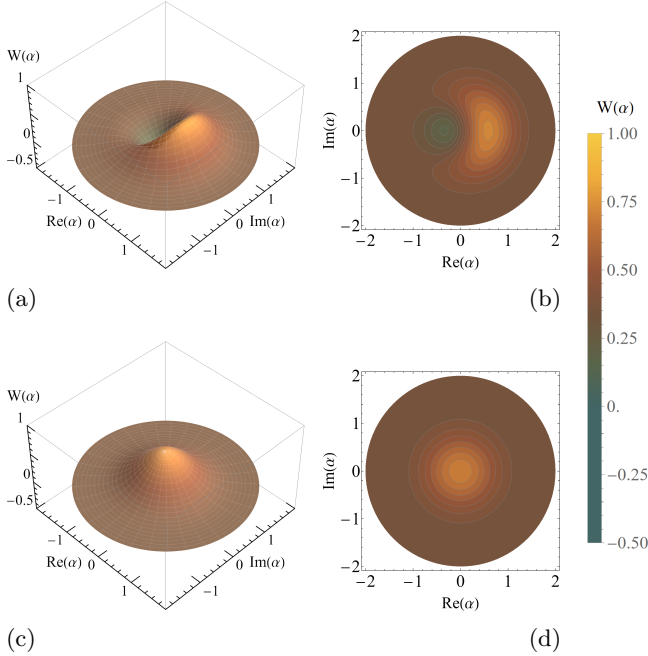


FIG. 3. Time evolution of the calculated Wigner function  $W(\alpha)$ . For all panels,  $T_1 = 5/\omega_0$ . Panels (a) and (b) show  $W(\alpha)$  at  $t = 0$ . Panels (c) and (d) show  $W(\alpha)$  at time  $t = 5T_1$ . A single color bar applies to both panels (b) and (d).

*Readout modalities* – We propose three different readout schemes (details in [Appendices A, B, C](#)).

(a) *AFM deflection*. Immediately after the Ramsey sequence, the CNT displacement is demodulated with the AFM to extract the quadrature signal and thereby extract  $P_1$  via the calibrated  $\pi/2$  mapping. The same Ramsey sweep that yields the fringe frequency  $\Delta$  and envelope  $T_2$  sets the AFM timing and pulse areas. Free ringdown of the demodulated signal gives  $T_1$  [14]. This purely

mechanical channel provides a direct population readout compatible with the Wigner tomography displacements. (b) *Dispersive CPB readout*. A Cooper-pair box dispersively coupled to the CNT acquires a phonon-number dependent phase [1, 4]. In the dispersive regime, the effective shift per phonon  $\chi$  maps parity to the CPB phase during a calibrated delay window  $t_\pi = \pi/\chi$ . The final CPB population after  $\{\pi/2, t_\pi, -\pi/2\}$  reads out  $P_1(\alpha)$  (see [Appendix B](#)). The phase  $\phi_d$  is set by the same Ramsey sequence, and the contrast is bounded by  $T_2$ .

(c) *Dispersive cavity readout*. A microwave cavity used as a phase-sensitive probe resolves the state mapped by the Ramsey sequence, either via a qubit-cavity dispersive pull or a direct mechanical dispersive shift [27, 28]. Coupling the CNT to the cavity produces a dispersive shift  $\pm\chi_c$  of the cavity frequency [29–31]. Homodyne detection resolves  $|0\rangle$  vs  $|1\rangle$  and converts the Ramsey outcome into a voltage (see [Appendix C](#)). Combined with the parity mapping this returns  $W(\alpha)$ .

All three methods share the same all-mechanical basic controls (AFM  $\pi/2$  rotations and displacements), extending the Ramsey interferometer into a full, state-resolved characterization of the phase space.

*Estimated device parameters* – Using the Euler–Bernoulli beam model for a doubly clamped thin-walled CNT of length  $L$  and radius  $r$ , the fundamental flexural frequency is  $\omega_0 = (\beta_1^2 r/L^2) \sqrt{E/2\rho}$ , with elastic modulus  $E \simeq 1\text{TPa}$ , density  $\rho \simeq 2200\text{ kg/m}^3$ , and  $\beta_1 \simeq 4.73$  [11]. The zero-point motion is  $x_{\text{zpf}} = \sqrt{\hbar/(2m_{\text{eff}} \cdot \omega_0)}$ . A resonant AFM force  $F(t)$  couples as  $-F(t)x$ , giving a Rabi frequency  $\Omega_R(t) = F(t)x_{\text{zpf}}/\hbar$ . To realize a  $\pi/2$  pulse of duration  $t_{\pi/2}$  one requires  $\Omega_R = \pi/(2t_{\pi/2})$  and therefore an applied force  $F_{\pi/2} \simeq \pi\hbar/(2t_{\pi/2} \cdot x_{\text{zpf}})$ . Thus, the force scale is set by  $x_{\text{zpf}}$  (decreasing as  $\sqrt{L}$  for fixed geometry) and is conveniently calibrated from a Rabi scan. Ramsey fringes yield the detuning  $\Delta$  and transverse coherence time  $T_2$ . Ringdown of the demodulated AFM signal returns  $T_1 = Q/\omega_0$ . Taking  $Q = 10^4$  (reported for suspended CNTs at tens of mK [32, 33]), and  $t_{\pi/2} = 100\text{ ns}$  the parameters scalings with CNT length  $L$  are summarized in Table I below [20]:

$L$ (nm)	$\omega_0/2\pi$ (MHz)	$x_{\text{zpf}}$ (pm)	$F_{\pi/2}$ (fN)	$T_1$ ( $\mu\text{s}$ )	$T_2$ ( $\mu\text{s}$ )
100	5370	2.14	0.77	0.29	0.58
500	221	4.79	0.35	7.4	14.8
1000	54	6.78	0.24	29.6	59.2

TABLE I. Representative parameters as a function of CNT length. Calculated values use  $Q = 10^4$ ,  $t_{\pi/2} = 100\text{ ns}$  and the Euler–Bernoulli beam model discussed in the main text. Here  $T_2 \simeq 2T_1$  assuming negligible pure dephasing.

Because the force required for  $\pi/2$  pulses scales as  $F_{\pi/2} \propto L^{-1/2}$  [20], mechanically driven rotations require a weaker drive in longer tubes. For fixed  $Q$  and negligible pure dephasing, the energy-relaxation time grows



as  $T_1 = Q/\omega_0 \propto L^2$ . The trade-off is a lower  $\omega_0$  (hence higher thermal occupation at a given temperature) for larger  $L$ . Short CNTs favor ground-state occupation at 50 mK, whereas longer CNTs favor extended coherence. The table quantifies this balance.

We introduced a minimal, all-mechanical platform in which a suspended CNT, driven and sensed by an AFM tip, enables coherent control and full quantum-state reconstruction of a mesoscopic mechanical mode. Calibrated AFM impulses serve both as  $\pi/2$  rotations for Rabi/Ramsey spectroscopy and as phase-space displacements for displaced-parity Wigner tomography, unifying preparation, control, and readout without on-chip microwaves or optical fields. Within a GKSL master-equation framework we connect directly measured signals to relaxation and dephasing times ( $T_1, T_2$ ). Ramsey fringes yield the excited state probability  $P_1^R(\tau)$ , while displaced-parity mapping returns the Wigner function  $W(\alpha)$  point-by-point, with no inverse reconstruction. Quantitative estimates place the required forces and timescales within current experimental capabilities. The same Ramsey sequence that calibrates the AFM drive also implements phase-coherent parity mapping for tomography. Regions with negative  $W(\alpha)$  reveal non-classical motion, while their decay diagnoses environmental decoherence. Compatible with direct AFM deflection, CPB-based, and cavity-based readouts, this approach opens a practical route to state-resolved decoherence studies and quantum control in CNT resonators, and is readily transferable to other nanomechanical platforms for non-Gaussian state preparation and quantum-enhanced sensing.

*Acknowledgments.* CS acknowledges support for this work from a Tufts Faculty Research Award (FRAC).

---

\* cstaii01@tufts.edu

- [1] A. D. Armour, M. P. Blencowe, and K. C. Schwab, Entanglement and Decoherence of a Micromechanical Resonator via Coupling to a Cooper-Pair Box, *Physical Review Letters* **88**, 148301 (2002).
- [2] N. R. Lee, Y. Guo, A. Y. Cleland, E. A. Wollack, R. G. Gruenke, T. Makihara, Z. Wang, T. Rajabzadeh, W. Jiang, F. M. Mayor, P. Arrangoiz-Arriola, C. J. Sabaalis, and A. H. Safavi-Naeini, Strong Dispersive Coupling Between a Mechanical Resonator and a Fluxonium Superconducting Qubit, *PRX Quantum* **4**, 040342 (2023).
- [3] K. C. Schwab and M. L. Roukes, Putting Mechanics into Quantum Mechanics, *Physics Today* **58**, 36 (2005).
- [4] M. Blencowe, Quantum electromechanical systems, *Physics Reports* **395**, 159 (2004).
- [5] C. Samanta, S. L. De Bonis, C. B. Møller, R. Tormo-Queralt, W. Yang, C. Urgell, B. Stamenic, B. Thibeault, Y. Jin, D. A. Czaplewski, F. Pistolesi, and A. Bachtold, Nonlinear nanomechanical resonators approaching the quantum ground state, *Nature Physics* **19**, 1340 (2023).
- [6] M. D. LaHaye, O. Buu, B. Camarota, and K. C. Schwab, Approaching the quantum limit of a nanomechanical resonator, *Science* **304**, 74 (2004).
- [7] L. G. Remus, M. P. Blencowe, and Y. Tanaka, Damping and decoherence of a nanomechanical resonator due to a few two-level systems, *Physical Review B* **80**, 174103 (2009).
- [8] E. A. Wollack, A. Y. Cleland, R. G. Gruenke, Z. Wang, P. Arrangoiz-Arriola, and A. H. Safavi-Naeini, Quantum state preparation and tomography of entangled mechanical resonators, *Nature* **604**, 463 (2022).
- [9] M. Schlosshauer, *Decoherence and the Quantum-To-Classical Transition*, Frontiers Collection (Springer Berlin Heidelberg, Berlin, Heidelberg, 2007).
- [10] V. Sazonova, Y. Yaish, H. Ustünel, D. Roundy, T. A. Arias, and P. L. McEuen, A tunable carbon nanotube electromechanical oscillator, *Nature* **431**, 284 (2004).
- [11] D. Garcia-Sanchez, A. San Paulo, M. J. Esplandiu, F. Perez-Murano, L. Forró, A. Aguasca, and A. Bachtold, Mechanical Detection of Carbon Nanotube Resonator Vibrations, *Physical Review Letters* **99**, 085501 (2007).
- [12] A. K. Hüttel, M. Poot, B. Witkamp, and H. S. J. van der Zant, Nanoelectromechanics of suspended carbon nanotubes, *New Journal of Physics* **10**, 095003 (2008).
- [13] A. Tavernarakis, A. Stavrinadis, A. Nowak, I. Tsioutsios, A. Bachtold, and P. Verlot, Optomechanics with a hybrid carbon nanotube resonator, *Nature Communications* **9**, 662 (2018).
- [14] B. H. Schneider, V. Singh, W. J. Venstra, H. B. Meerwaldt, and G. A. Steele, Observation of decoherence in a carbon nanotube mechanical resonator, *Nature Communications* **5**, 5819 (2014).
- [15] A. Pályi, P. R. Struck, M. Rudner, K. Flensberg, and G. Burkard, Spin-Orbit-Induced Strong Coupling of a Single Spin to a Nanomechanical Resonator, *Physical Review Letters* **108**, 206811 (2012).
- [16] X. Wang, A. Miranowicz, H.-R. Li, and F. Nori, Hybrid quantum device with a carbon nanotube and a flux qubit for dissipative quantum engineering, *Physical Review B* **95**, 205415 (2017).
- [17] H. Wang and G. Burkard, Creating arbitrary quantum vibrational states in a carbon nanotube, *Physical Review B* **94**, 205413 (2016).
- [18] I. Wilson-Rae, N. Nooshi, W. Zwerger, and T. J. Kippenberg, Theory of ground state cooling of a mechanical oscillator using dynamical backaction, *Phys. Rev. Lett.* **99**, 093901 (2007).
- [19] C. Urgell, W. Yang, S. L. De Bonis, C. Samanta, M. J. Esplandiu, Q. Dong, Y. Jin, and A. Bachtold, Cooling and self-oscillation in a nanotube electromechanical resonator, *Nat. Phys.* **16**, 32 (2020).
- [20] See Supplemental Material at [URL], which provides detailed derivations of the system Hamiltonian for the AFM-driven CNT, the GKSL master equation and Bloch equations, solutions of the Bloch equations under dissipation (Rabi and Ramsey dynamics), calculation of the Wigner function for the CNT coupled to the environment, and estimates of representative device parameters.
- [21] H.-P. Breuer and F. Petruccione, *The Theory of Open Quantum Systems*, 1st ed. (Clarendon Press, Oxford, 2009).
- [22] P. Lougovski, E. Solano, Z. M. Zhang, H. Walther, H. Mack, and W. P. Schleich, Fresnel Representation of the Wigner Function: An Operational Approach, *Physi-*

- cal Review Letters **91**, 010401 (2003).
- [23] P. Bertet, A. Auffeves, P. Maioli, S. Osnaghi, T. Meunier, M. Brune, J. M. Raimond, and S. Haroche, Direct Measurement of the Wigner Function of a One-Photon Fock State in a Cavity, *Physical Review Letters* **89**, 200402 (2002).
- [24] D. Leibfried, D. M. Meekhof, B. E. King, C. Monroe, W. M. Itano, and D. J. Wineland, Experimental Determination of the Motional Quantum State of a Trapped Atom, *Physical Review Letters* **77**, 4281 (1996).
- [25] D. V. Karlovets and V. G. Serbo, Possibility to Probe Negative Values of a Wigner Function in Scattering of a Coherent Superposition of Electronic Wave Packets by Atoms, *Physical Review Letters* **119**, 173601 (2017).
- [26] J. Weinbub and D. K. Ferry, Recent advances in Wigner function approaches, *Applied Physics Reviews* **5**, 041104 (2018).
- [27] C. A. Regal, J. D. Teufel, and K. W. Lehnert, Measuring nanomechanical motion with a microwave cavity interferometer, *Nature Physics* **4**, 555 (2008).
- [28] J. D. Teufel, D. Li, M. S. Allman, K. Cicak, A. J. Sirois, J. D. Whittaker, and R. W. Simmonds, Circuit cavity electromechanics in the strong-coupling regime, *Nature* **471**, 204 (2011).
- [29] V. Ranjan, G. Puebla-Hellmann, M. Jung, T. Hasler, A. Nunnenkamp, M. Muoth, C. Hierold, A. Wallraff, and C. Schönerberger, Clean carbon nanotubes coupled to superconducting impedance-matching circuits, *Nature Communications* **6**, 7165 (2015).
- [30] M. Aspelmeyer, T. J. Kippenberg, and F. Marquardt, Cavity optomechanics, *Reviews of Modern Physics* **86**, 1391 (2014).
- [31] S. Blien, P. Steger, N. Hüttner, R. Graaf, and A. K. Hüttel, Quantum capacitance mediated carbon nanotube optomechanics, *Nature Communications* **11**, 1636 (2020).
- [32] G. A. Steele, A. K. Hüttel, B. Witkamp, M. Poot, H. B. Meerwaldt, L. P. Kouwenhoven, and H. S. J. van der Zant, Strong coupling between single-electron tunneling and nanomechanical motion, *Science* **325**, 1103 (2009).
- [33] M. Cirio, G. K. Brennen, and J. Twamley, Quantum magnetomechanics: Ultrahigh- $q$ -levitated mechanical oscillators, *Phys. Rev. Lett.* **109**, 147206 (2012).
- [34] A. Blais, R.-S. Huang, A. Wallraff, S. M. Girvin, and R. J. Schoelkopf, Cavity quantum electrodynamics for superconducting electrical circuits: An architecture for quantum computation, *Physical Review A* **69**, 062320 (2004).
- [35] A. Blais, A. L. Grimsmo, S. M. Girvin, and A. Wallraff, Circuit quantum electrodynamics, *Reviews of Modern Physics* **93**, 025005 (2021).
- [36] M. Boissonneault, J. M. Gambetta, and A. Blais, Dispersive regime of circuit QED: Photon-dependent qubit dephasing and relaxation rates, *Physical Review A* **79**, 013819 (2009).
- [37] D. Zueco, G. M. Reuther, S. Kohler, and P. Hänggi, Qubit-oscillator dynamics in the dispersive regime: Analytical theory beyond the rotating-wave approximation, *Physical Review A* **80**, 033846 (2009).
- [38] M. D. LaHaye, J. Suh, P. M. Echternach, K. C. Schwab, and M. L. Roukes, Nanomechanical measurements of a superconducting qubit, *Nature* **459**, 960 (2009).
- [39] J.-M. Pirkkalainen, S. U. Cho, F. Massel, J. Tuorila, T. T. Heikkilä, P. J. Hakonen, and M. A. Sillanpää, Cavity optomechanics mediated by a quantum two-level system, *Nature Communications* **6**, 6981 (2015).
- [40] A. Eichler, J. Moser, J. Chaste, M. Zdrojek, I. Wilson-Rae, and A. Bachtold, Nonlinear damping in mechanical resonators made from carbon nanotubes and graphene, *Nature Nanotechnology* **6**, 339 (2011).
- [41] W. Cui, Z. Zhang, and K. Mølmer, Feedback control of rabi oscillations in circuit qed, *Physical Review A* **88**, 063823 (2013).
- [42] D. Ristè, J. G. van Leeuwen, H.-S. Ku, K. W. Lehnert, and L. DiCarlo, Initialization by measurement of a superconducting quantum bit circuit, *Physical Review Letters* **109**, 050507 (2012).

## END MATTER

*Appendix A: AFM deflection and direct population readout* — Immediately after the Ramsey sequence, the CNT displacement is transduced by the AFM probe (optical/electrical deflection or weak probe force) described by

$$H_{\text{meas}}(t) = -F_{\text{probe}}(t)x = -F_{\text{probe}}(t)x_{\text{zpf}}(a + a^\dagger). \quad (\text{A1})$$

Linear demodulation of the deflection quadrature distinguishes  $|1\rangle$  from  $|0\rangle$ , returning  $P_1$  in a single readout. The mechanical ringdown of the demodulated signal yields the longitudinal relaxation time  $T_1$ , while sweeping the Ramsey delay  $\tau$  gives the detuning frequency  $\Delta$  and phase coherence time  $T_2$ . This channel is used to measure population and characterize decoherence. Practical implementation follows the Ramsey calibration: (i) set  $\omega_d \approx \omega_0$  and determine  $\Omega_R$  via a Rabi scan; (ii) choose  $t_{\pi/2} = \pi/(2\Omega_R)$ , (iii) synchronize two identical  $\pi/2$  pulses with programmable delay  $\tau$ , and (iv) demodulate the AFM signal during a short integration window after the second pulse. Typical operating times are  $t_{\pi/2} \sim 0.1\text{--}0.3\ \mu\text{s}$ ,  $\tau = 0.1\text{--}50\ \mu\text{s}$ . Readout is performed via lock-in or IQ demodulation referenced to the drive frequency  $\omega_d$ .

*Appendix B: Dispersive CPB readout and parity mapping* — A Cooper-pair box dispersively coupled to the CNT implements a phase proportional to the phonon-number operator  $\hat{n} = a^\dagger a$  during the Ramsey free-evolution window [1, 4].

The Jaynes-Cummings interaction is

$$\frac{H}{\hbar} = \omega_0 a^\dagger a + \frac{\omega_q}{2} \sigma_z + g_m (a \sigma_+ + a^\dagger \sigma_-), \quad (\text{B1})$$

where  $\omega_0$  is the CNT flexural-mode frequency,  $\omega_q$  is the CPB qubit transition frequency, and  $g_m$  is the CPB-CNT coupling. The CPB-CNT mechanical-mode detuning is  $\Delta_q \equiv \omega_q - \omega_0$ . For  $|\Delta_q| \gg g_m$ , the interaction reduces to the dispersive Hamiltonian [34–37]:

$$\frac{H_{\text{int}}^{(\text{CPB})}}{\hbar} \simeq \chi a^\dagger a \frac{\sigma_z}{2}, \quad \chi \simeq \frac{2g_m^2}{\Delta_q}. \quad (\text{B2})$$

Mechanical implementations of such dispersive couplings have been demonstrated with CPB/transmon devices [2, 38, 39]. During a calibrated window  $t_\pi = \pi/\chi$ , the CPB acquires the number-dependent phase  $\chi t_\pi \hat{n}$ , implementing  $e^{i\pi\hat{n}}$ . When the Ramsey sequence is preceded by a mechanical displacement  $D(\alpha)$  and performed with the pulse sequence  $\{\pi/2, t_\pi, -\pi/2\}$  (where  $-\pi/2$  denotes a  $\pi/2$  rotation with a  $\pi$ -phase flip of the drive), the excited-state probability encodes the displaced parity signal as given in Eq. (13) in the main text. High-contrast mapping requires  $2\pi/\omega_0 \ll t_\pi \ll T_2$ , and dephasing during  $t_\pi$  limits the contrast.

In a purely mechanical variant, a weak Duffing (self-Kerr) term arising from tension-induced geometric effects and/or electrostatic forces [34–37, 40] yields an effective number-dependent phase rate  $\chi$  and realizes the same parity gate  $e^{i\pi\hat{n}}$ , with  $t_\pi = \pi/\chi$ . For typical CNT resonators ( $L \sim 0.1\text{--}1\ \mu\text{m}$ ), this corresponds to  $t_\pi \sim 1\text{--}20\ \mu\text{s}$ .

*Appendix C: Dispersive cavity readout* — A microwave cavity operated in the dispersive regime provides phase-sensitive readout of the CPB qubit state during the Ramsey sequence. The effective readout Hamiltonian is

$$\frac{H_{\text{read}}}{\hbar} = \omega_c a_c^\dagger a_c + \frac{\tilde{\omega}_q}{2} \sigma_z + \chi_c a_c^\dagger a_c \frac{\sigma_z}{2}. \quad (\text{C1})$$

Here,  $\omega_c$  is the bare cavity angular frequency;  $a_c$  ( $a_c^\dagger$ ) annihilates (creates) a cavity photon;  $\tilde{\omega}_q$  is the dressed CPB qubit transition frequency (including static Lamb/AC-Stark shifts); and  $\chi_c$  is the dispersive coupling (“cavity pull”) that produces a CPB state-dependent cavity shift  $\omega_c \rightarrow \omega_c \pm \chi_c/2$  for  $\sigma_z = \pm 1$  [34–37].

*Homodyne detection.* The cavity is driven near  $\omega_c$  and the transmitted (or reflected) field is routed through cryogenic circulators/isolators and a high electron mobility transistor (HEMT) low-noise amplifier [41, 42]. The signal is mixed with a local oscillator (LO) phase-locked to the cavity probe in an IQ mixer to yield base-band voltages  $I(t)$  and  $Q(t)$ . The instantaneous phase  $\phi(t) = \arctan[Q(t)/I(t)]$  (or an appropriate quadrature) tracks the CPB qubit observable  $\sigma_z$ , since the CPB state-dependent pull  $\pm\chi_c/2$  rotates the cavity response in the complex plane [41, 42]. Integration over a window set by the cavity linewidth provides the Ramsey or parity-mapped population used in the analysis.

*Direct mechanics-cavity option.* As an alternative to CPB-based readout, one may couple the cavity directly to the CNT mode to produce either a cross-Kerr interaction [30]:

$$\frac{H_{\text{int}}^{(\text{mc})}}{\hbar} \simeq \chi_{mc} a^\dagger a_c^\dagger a_c, \quad (\text{C2})$$

or a radiation-pressure interaction [30, 35]:

$$\frac{H_{\text{rp}}}{\hbar} = -g_0 a_c^\dagger a_c (a + a^\dagger), \quad (\text{C3})$$

During the Ramsey free-evolution window, these couplings generate an effective phase rate  $\chi_{\text{eff}}$  proportional to the CNT phonon number  $\hat{n}$ , so the same parity gate  $e^{i\pi\hat{n}}$  is realized by choosing  $t_\pi = \pi/\chi_{\text{eff}}$ . The tomography framework and normalization are the same as described in Appendix B.

*Appendix D: Practical timing, calibration, and acquisition* — Mechanical rotations are kept short ( $t_{\pi/2} \ll \tau, T_2$ ) to minimize pulse-induced dephasing. The relative phase of the second  $\pi/2$  rotation is set either by a  $\pi$  phase flip of the drive or by a half-period timing slip  $t = \pi/\omega_d$ . The parity-mapping window  $t_\pi$  is chosen using an estimate of  $\chi$  and then fine-tuned by maximizing contrast, subject to the condition  $2\pi/\omega_0 \ll t_\pi \ll T_2$  (see Appendix B). The Ramsey population  $P_1^R(\tau)$  is fitted to the expressions given in the main text (Eq. (10)).

Calibration follows the sequence summarized in Appendix A: Rabi scans set  $\Omega_R$  and  $t_{\pi/2}$ , Ramsey scans determine  $\Delta$  and  $T_2$ , and mechanical ringdown yields  $T_1$ . The displacement for  $D(\alpha)$  is obtained from the small-signal transfer function. The waveform generator, digitizer, and LO share a common frequency reference. Hardware gating minimizes relative jitter and slow LO-phase drift is tracked with interleaved references [41, 42].

For cavity readout, the I/Q record (Appendix C) is integrated with a matched filter over a window on the order of the cavity photon lifetime, chosen to remain well within the CPB  $T_1$ . For AFM deflection readout, the demodulated quadrature at  $\omega_d$  is integrated over a short  $\mu\text{s}$ -scale window placed after the second pulse to avoid drive transients, while remaining much shorter than  $T_1$ .

## Supplemental Material for Quantum Tomography of Suspended Carbon Nanotubes

### This PDF file includes:

- S1. System Hamiltonian for the AFM-driven CNT
- S2. GKSL Master Equation and Bloch Equations
- S3. Solutions of the Bloch Equations under Dissipation (Rabi and Ramsey)
- S4. Wigner Function for the CNT Coupled to the Environment
- S5. Calculation of Representative Device Parameters

### S1. SYSTEM HAMILTONIAN FOR THE AFM-DRIVEN CNT

*Physical system.* A single-wall carbon nanotube (CNT) of length  $L$  is doubly clamped across a nanofabricated trench (Fig. 1 in the main text). At cryogenic temperature ( $\sim 50\text{mK}$ ) its fundamental flexural mode behaves as a quantized harmonic oscillator of angular frequency  $\omega_0$ , with only the ground and first excited states occupied. By restricting the Hilbert space to the lowest two states  $\{|0\rangle, |1\rangle\}$ , the CNT can be treated as an effective two-level system (TLS), described using the Pauli operators  $\sigma_z = |1\rangle\langle 1| - |0\rangle\langle 0|$  and  $\sigma_x = |0\rangle\langle 1| + |1\rangle\langle 0|$ . The Hamiltonian for the undriven TLS is

$$H_0 = \frac{\hbar\omega_0}{2} \sigma_z, \quad (14)$$

*Mechanical drive.* An atomic force microscope (AFM) tip positioned near the CNT exerts a time-dependent force

$$F(t) = F_0 \cos(\omega_d t). \quad (15)$$

which couples to the nanotube displacement  $\hat{x} = x_{\text{zpf}}(a + a^\dagger)$ . Projecting onto the two-level subspace gives,  $\hat{x} \rightarrow x_{\text{zpf}}\sigma_x$ , so the time-dependent drive Hamiltonian is

$$H_{\text{drv}}(t) = F_0 x_{\text{zpf}} \cos(\omega_d t) \sigma_x \equiv \hbar g \cos(\omega_d t) \sigma_x, \quad g = \frac{F_0 x_{\text{zpf}}}{\hbar}. \quad (16)$$

*Environmental bath.* The surrounding bosonic environment is modeled as a set of independent harmonic oscillators in thermal equilibrium,  $H_B = \sum_k \hbar\omega_k b_k^\dagger b_k$ . To lowest order, the CNT-environment coupling is described by the Hamiltonian [21]

$$H_I = \hbar\sigma_z \sum_k g_k (b_k^\dagger + b_k), \quad (17)$$

which induces both energy relaxation and dephasing. The coefficients  $g_k$  in Eq. (17) represent coupling to bath mode  $k$  with frequency  $\omega_k$ .

Collecting the above equations we obtain the **laboratory-frame Hamiltonian**:

$$H_{\text{lab}} = \frac{\hbar\omega_0}{2} \sigma_z + \hbar g \cos(\omega_d t) \sigma_x + \sum_k \hbar\omega_k b_k^\dagger b_k + \hbar\sigma_z \sum_k g_k (b_k^\dagger + b_k). \quad (18)$$

This expression represents the full Hamiltonian in the laboratory frame, containing a harmonically modulated  $\sigma_x$  drive and longitudinal coupling to a bosonic bath.

*System Hamiltonian in the rotating wave approximation.* For weak driving,  $g \ll \omega_0$  we transform the above Hamiltonian into a rotating frame and use the rotating wave approximation (RWA). First, introduce the unitary operator

$$U(t) = \exp\left(i\frac{\omega_d t}{2} \sigma_z\right), \quad (19)$$

which rotates the TLS about the  $z$ -axis at the drive frequency. Operators transform according to  $\tilde{A}(t) = U(t) A U^\dagger(t)$  and by applying Eq. (19) to the free and drive Hamiltonians we get:

$$U H_0 U^\dagger = \frac{\hbar}{2} (\omega_0 - \omega_d) \sigma_z \equiv \frac{\hbar\Delta}{2} \sigma_z, \quad (20)$$

$$U H_{\text{drv}}(t) U^\dagger = \hbar g \cos(\omega_d t) [\sigma_x \cos(\omega_d t) + \sigma_y \sin(\omega_d t)], \quad (21)$$



where  $\Delta \equiv \omega_0 - \omega_d$  is the detuning. Expanding the product of cosines/sines yields terms and applying the RWA we obtain the static contribution:

$$UH_{\text{drv}}(t)U^\dagger \xrightarrow{\text{RWA}} = \frac{\hbar\Omega_R}{2} \sigma_x,$$

with the *Rabi frequency*:  $\Omega_R = F_0 x_{\text{zpf}}/\hbar$ . Because  $U(t)$  commutes with  $H_B$  and  $\sigma_z$ , the environment Hamiltonian is *unchanged*:  $\tilde{H}_{\text{env}} = H_B + H_I$ . Collecting all the terms we arrive at the **rotating-frame Hamiltonian**:

$$\tilde{H} = \frac{\hbar\Delta}{2} \sigma_z + \frac{\hbar\Omega_R}{2} \sigma_x + \sum_k \hbar\omega_k b_k^\dagger b_k + \hbar\sigma_z \sum_k g_k (b_k^\dagger + b_k). \quad (22)$$

*Physical interpretation.* Because the AFM force couples linearly to the displacement operator, and only the co-rotating component of the drive survives in the RWA, the single-phonon coupling strength  $g$  appears directly as the coefficient of the transverse Pauli operator  $\sigma_x$  in the Hamiltonian. Thus, the AFM drive injects energy at a rate  $F_0 x_{\text{zpf}}$  per quantum, setting a natural frequency scale. When the drive is *on resonance* ( $\Delta = 0$ ), the nanotube oscillates between  $|0\rangle$  and  $|1\rangle$  at the natural frequency scale given by the Rabi frequency  $\Omega_R$ . Off resonance ( $\Delta \neq 0$ ) the oscillation frequency generalizes to  $\Omega = \sqrt{\Delta^2 + \Omega_R^2}$ .

The bath coupling (last term in Eq. (22)) produces both energy relaxation and dephasing, which in the Born–Markov treatment leads to the Bloch relaxation and phase-coherence rates  $\Gamma_1$  and  $\Gamma_2$ , discussed below. Eq. (22) is the starting point for analyzing Ramsey and Wigner-tomography protocols for the mechanically driven CNT resonator.

## S2. GKSL MASTER EQUATION AND BLOCH EQUATIONS

After transforming to the drive rotating frame and making the rotating-wave approximation (RWA), the Hamiltonian reads

$$\tilde{H} = H_S + H_B + H_I \quad (23)$$

with

$$H_S = \frac{\hbar\Delta}{2} \sigma_z + \frac{\hbar\Omega_R}{2} \sigma_x, \quad \Delta = \omega_0 - \omega_d, \quad (24a)$$

$$H_B = \sum_k \hbar\omega_k b_k^\dagger b_k, \quad (24b)$$

$$H_I = \hbar\sigma_z \sum_k g_k (b_k^\dagger + b_k). \quad (24c)$$

In the interaction picture generated by  $H_S + H_B$  the density matrix transforms as [21]:  $\tilde{\rho}_I(t) = e^{i(H_S+H_B)t/\hbar} \tilde{\rho}(t) e^{-i(H_S+H_B)t/\hbar}$ , and the interaction Hamiltonian becomes:

$$H_I(t) = \hbar\sigma_z(t)B(t), \quad \begin{cases} \sigma_z(t) = e^{iH_S t/\hbar} \sigma_z e^{-iH_S t/\hbar}, \\ B(t) = \sum_k g_k (b_k^\dagger e^{i\omega_k t} + b_k e^{-i\omega_k t}). \end{cases} \quad (25)$$

*Born–Markov assumptions:*

1. *Born approximation*: the composite state factorizes,  $\tilde{\rho}_I(t) \approx \rho_S(t) \otimes \rho_B$ , where  $\rho_B = e^{-H_B/k_B T} / \text{Tr}(e^{-H_B/k_B T})$  is stationary.
2. *Markov approximation*: bath correlations decay much faster than the timescale over which  $\rho_S(t)$  changes appreciably.
3. *RWA approximation*: retain only terms oscillating slowly compared with the TLS transition frequencies.

These assumptions lead to the following time evolution equation for the reduced density matrix [9, 21]:

$$\dot{\rho}_S(t) = -\frac{1}{\hbar^2} \int_0^\infty d\tau \text{Tr}_B \left[ H_I(t), [H_I(t-\tau), \rho_S(t) \otimes \rho_B] \right]. \quad (26)$$

Next, we define the bath correlation function  $C(\tau) = \langle B(\tau)B(0) \rangle_B$ , and write  $\sigma_z(t)$  in the energy basis ( $\hbar\Omega = \sqrt{\Delta^2 + \Omega_R^2}$ ),  $\sigma_z(t) = \sum_{\omega=0,\pm\Omega} e^{-i\omega t} A_\omega$ , where  $A_0 = (\Delta/\Omega)\sigma_z^{(e)}$  and  $A_{\pm\Omega} = (\Omega_R/2\Omega)\sigma_{\pm}^{(e)}$ . Substituting into Eq. (26) and performing the  $\tau$ -integral one arrives at the standard Gorini–Kossakowski–Sudarshan–Lindblad (GKSL) equation [9, 21]:

$$\dot{\rho}_S = -\frac{i}{\hbar} [H_S, \rho_S] + \gamma_\downarrow \mathcal{D}[\sigma_-] \rho_S + \gamma_\uparrow \mathcal{D}[\sigma_+] \rho_S + \gamma_\varphi \mathcal{D}[\sigma_z] \rho_S, \quad (27)$$

with the *dissipator*:

$$\mathcal{D}[\sigma] \rho_S \equiv \sigma \rho_S \sigma^\dagger - \frac{1}{2} \{ \sigma^\dagger \sigma, \rho_S \}. \quad (28)$$

*Physical interpretation.* The system Hamiltonian  $H_S$  in Eq. (27) describes unitary evolution generated solely by the system degrees of freedom (the driven TLS CNT resonator). The commutator  $-i[H_S, \rho]/\hbar$  is the familiar Liouville–vonNeumann term  $\partial_t \rho = -i[H_S, \rho]/\hbar$  for an isolated quantum system. The dissipator in Eq. (28) generates irreversible, stochastic jumps associated with processes in the environment. The competition between coherent drive and dissipative processes sets the visibility of Rabi oscillations, Ramsey fringes, and Wigner-function negativity in the nanotube qubit. Each sum term in Eq. (27) has the structure  $\gamma_j \mathcal{D}[\sigma_j] \rho_S$  with the dissipator  $\mathcal{D}[\sigma] \rho_S$  defined in Eq. (28). The  $\sigma$  matrices represent the Lindblad operators, and capture specific physical processes (population jumps, phase kiks) induced by the environment:

- $\sigma_- (= |0\rangle\langle 1|)$  : energy relaxation ( $|1\rangle \rightarrow |0\rangle$ ).
- $\sigma_+ (= |1\rangle\langle 0|)$  : thermal excitation ( $|0\rangle \rightarrow |1\rangle$ ).
- $\sigma_z$  : pure dephasing (phase pulses that leave populations unchanged).

The gain term  $\sigma \rho_S \sigma^\dagger$  in Eq. (28) adds population or coherence consistent with the jump. The loss term  $-\frac{1}{2} \{ \sigma^\dagger \sigma, \rho_S \}$  subtracts terms such that the total evolution preserves  $\text{Tr} \rho_S = 1$ .

The dissipative rates  $\gamma_\uparrow$ ,  $\gamma_\downarrow$ , and  $\gamma_\varphi$  are non-negative and have dimensions of inverse time. They are set by the bath spectral density and temperature. For a transition at frequency  $\omega_0$  [9, 21]:

$$\gamma_\uparrow = 2\pi J(\omega_0) n(\omega_0), \quad \gamma_\downarrow = 2\pi J(\omega_0) [n(\omega_0) + 1],$$

where  $J(\omega) = 2\alpha\omega e^{-\omega/\omega_c}$  is the Ohmic spectral density (with dimensionless coupling  $\alpha$  and cutoff  $\omega_c$ ), and  $n(\omega) = [e^{\hbar\omega/k_B T} - 1]^{-1}$  is the thermal occupation number. The Bloch decay parameters are  $\Gamma_1 \equiv \gamma_\downarrow + \gamma_\uparrow$  and  $\Gamma_2 \equiv \Gamma_1/2 + \gamma_\varphi$ . A pure-dephasing rate arises from slow longitudinal frequency noise and, for an Ohmic bath, scales as  $\gamma_\varphi \simeq 4\pi\alpha k_B T/\hbar$ . In the relaxation-limited regime (i.e., when slow longitudinal fluctuations are negligible on the experimental timescale), we have  $\gamma_\varphi \approx 0$  and thus  $\Gamma_2 = \Gamma_1/2$ .

*Derivation of the Bloch equations from the GKSL master equation.* The Bloch vector components are defined as [21]:

$$X \equiv \text{Tr}(\sigma_x \rho), \quad Y \equiv \text{Tr}(\sigma_y \rho), \quad Z \equiv \text{Tr}(\sigma_z \rho)$$

Equivalently we can write the reduced density matrix as:

$$\rho_S = \frac{1}{2} (\mathbb{1} + X\sigma_x + Y\sigma_y + Z\sigma_z). \quad (29)$$

By substituting the Bloch representation (Eq. (29)) into the GKSL equation (Eq. (27)) and explicitly evaluating each term in the dissipator (Eq. (28)) using the commutation relations  $[\sigma_i, \sigma_j] = 2i\varepsilon_{ijk}\sigma_k$ , one obtains, after straightforward algebra, the Bloch equations for a mechanically driven carbon nanotube coupled to its environment:

$$\begin{aligned}
\dot{X} &= -\left(\frac{1}{2}\gamma_{\downarrow} + \frac{1}{2}\gamma_{\uparrow} + \gamma_{\varphi}\right)X + \Delta Y, \\
\dot{Y} &= -\left(\frac{1}{2}\gamma_{\downarrow} + \frac{1}{2}\gamma_{\uparrow} + \gamma_{\varphi}\right)Y - \Delta X + \Omega_R Z, \\
\dot{Z} &= -(\gamma_{\downarrow} + \gamma_{\uparrow})Z - \Omega_R Y + (\gamma_{\uparrow} - \gamma_{\downarrow}).
\end{aligned} \tag{30}$$

All decay terms in Eq. (30) are written in terms of the physical rates  $\gamma_{\downarrow}$ ,  $\gamma_{\uparrow}$  (energy exchange) and  $\gamma_{\varphi}$  (pure dephasing), which determine the longitudinal relaxation time  $T_1$  and transverse coherence time  $T_2$ :

$$T_1 = \frac{1}{\gamma_{\downarrow} + \gamma_{\uparrow}}, \quad T_2 = \frac{1}{\frac{\gamma_{\downarrow} + \gamma_{\uparrow}}{2} + \gamma_{\varphi}}. \tag{31}$$

*Physical interpretation.* The longitudinal relaxation time  $T_1$  characterizes population relaxation towards thermal equilibrium, energy decay from  $|1\rangle$  to  $|0\rangle$  and thermal repopulation. Physically,  $T_1$  quantifies how rapidly an excited nanotube state  $|1\rangle$  decays to  $|0\rangle$  (via  $\gamma_{\downarrow}$ ) while the thermal bath repopulates  $|1\rangle$  with rate  $\gamma_{\uparrow}$ . The phase-coherence time  $T_2$ , governs the exponential decay of the off-diagonal density-matrix elements. In the relaxation-limited regime  $\gamma_{\varphi} \approx 0$ , and  $T_2 \simeq 2T_1$

By defining the thermal inversion  $Z_{\text{eq}} = -\tanh(\hbar\Omega/2k_B T) = (\gamma_{\uparrow} - \gamma_{\downarrow})/(\gamma_{\uparrow} + \gamma_{\downarrow})$ , the Bloch equations Eqs. (30) take the form given in the main text:

$$\dot{X} = -\Gamma_2 X + \Delta Y, \tag{32a}$$

$$\dot{Y} = -\Gamma_2 Y - \Delta X + \Omega_R Z, \tag{32b}$$

$$\dot{Z} = -\Gamma_1 (Z - Z_{\text{eq}}) - \Omega_R Y, \tag{32c}$$

with rates  $\Gamma_1 = \gamma_{\downarrow} + \gamma_{\uparrow}$ ,  $\Gamma_2 = \frac{\Gamma_1}{2} + \gamma_{\varphi}$ . The Rabi frequency for the mechanically driven CNT is  $\Omega_R = F_0 x_{\text{zpf}}/\hbar$ .

*In summary*, starting from the Hamiltonian in Eq. (23), the Born–Markov approximation yields the GKSL master equation Eq. (27). The resulting rates describe mechanical damping ( $\gamma_{\downarrow}$ ), thermal excitation ( $\gamma_{\uparrow}$ ) and low-frequency noise ( $\gamma_{\varphi}$ ), thereby establishing a quantitative connection between the microscopic properties of the environment and the observable relaxation and dephasing times for the mechanically driven CNT resonator.

### S3. SOLUTIONS OF THE BLOCH EQUATIONS UNDER DISSIPATION (RABI AND RAMSEY)

By choosing zero detuning  $\Delta = \omega_0 - \omega_d = 0$  and shift  $z(t) = Z(t) - Z_{\text{eq}}$ , Eqs. (32) become:

$$\dot{X} = -\Gamma_2 X, \tag{33a}$$

$$\dot{Y} = -\Gamma_2 Y + \Omega_R(z + Z_{\text{eq}}), \tag{33b}$$

$$\dot{z} = -\Gamma_1 z - \Omega_R Y, \tag{33c}$$

which are homogeneous in  $(Y, z)$  apart from the constant term  $\Omega_R Z_{\text{eq}}$ .

After eliminating  $X$  and  $Y$ , the  $Z$ -component satisfies the following equation:

$$\ddot{z} + 2\lambda\dot{z} + (\lambda^2 + \Omega_d^2)z = -\Omega_R^2 Z_{\text{eq}}, \tag{34}$$

with

$$\lambda \equiv \frac{\Gamma_1 + \Gamma_2}{2}, \quad \Omega_d \equiv \sqrt{\Omega_R^2 - \left(\frac{\Gamma_1 - \Gamma_2}{2}\right)^2},$$

The general solution of Eq. (34) is:

$$z(t) = -\frac{\Omega_R^2}{\lambda^2 + \Omega_d^2} Z_{\text{eq}} + e^{-\lambda t} [C_1 \cos(\Omega_d t) + C_2 \sin(\Omega_d t)]. \tag{35}$$

The physical  $Z$ -Bloch component is:

$$Z(t) = z(t) + Z_{\text{eq}}. \quad (36)$$

Once  $Z(t)$  is known, the probability of occupying the excited vibrational state  $|1\rangle$  is given by [21]:

$$P_1(t) = \frac{1 + Z(t)}{2}, \quad (P_0(t) = 1 - P_1(t) = \frac{1 - Z(t)}{2}), \quad (37)$$

*Solutions for initial ground state  $|0\rangle$ .* We assume the CNT is initially in the ground state  $|\psi(0)\rangle = |0\rangle$ , so the Bloch vector starts at the south pole:

$$Z(0) = -1 \implies z(0) = -1 - Z_{\text{eq}}, \quad \dot{z}(0) = \Gamma_1(1 + Z_{\text{eq}}). \quad (38)$$

Moreover, we assume that the system is at cryogenic temperatures ( $\sim 50\text{mK}$ ) such that  $Z_{\text{eq}} = -\tanh(\hbar\omega/2k_B T) \approx -1$ .

By substituting these conditions into the general solution in Eq. (35), we obtain the expression for the excited-state occupation probability given in the main text:

$$P_1(t) = \frac{\Omega_R^2}{2(\Omega_R^2 + \Gamma_1\Gamma_2)} \left[ 1 - e^{-(\Gamma_1 + \Gamma_2)t/2} \left( \cos(\Omega_d t) + \frac{\Gamma_1 - \Gamma_2}{2\Omega_d} \sin(\Omega_d t) \right) \right], \quad (39)$$

*Ramsey oscillations.* Assume the CNT starts in the ground state  $|\psi(0)\rangle = |0\rangle$ , with Bloch vector  $(0, 0, -1)$ . Consider two short AFM  $\pi/2$  pulses separated by a free-evolution interval  $\tau$ , and work in the short-pulse regime  $t_{\pi/2} = \frac{\pi}{2\Omega_R} \ll \tau, T_1, T_2$ , so dissipation during the pulses is negligible. Immediately after the first pulse the CNT is in the state  $|\psi(0^+)\rangle = \frac{1}{\sqrt{2}}(|0\rangle + |1\rangle)$ . We choose the phase of the first resonant  $\pi/2$  pulse such that the Bloch vector becomes:  $(1, 0, 0)$ . During the free interval  $\tau$  the drive is off,  $\Omega_R(t) = 0$ , and the Bloch equations (Eqs. 32) decouple. With initial condition  $(X, Y) = (1, 0)$  at  $t = 0$  one obtains

$$X(\tau) = e^{-\tau/T_2} \cos(\Delta\tau), \quad (40)$$

$$Y(\tau) = e^{-\tau/T_2} \sin(\Delta\tau), \quad (41)$$

independent of  $T_1$ . The longitudinal component  $Z(\tau)$  does not enter the ideal Ramsey signal below.

Let the second resonant  $\pi/2$  pulse have phase  $\phi_0$  (set by the programmed phase between the two AFM pulses). A  $\pi/2$  rotation about an equatorial axis with azimuth  $\phi_0$  maps the equatorial projection  $(X, Y)$  onto the  $Z$  axis according to

$$Z_f = X(\tau) \cos \phi_0 + Y(\tau) \sin \phi_0, \quad (42)$$

so the excited-state probability after the second pulse is

$$P_1^R(\tau) = \frac{1 + Z_f}{2}. \quad (43)$$

Substituting Eqs. (40)–(41) into Eq. (42) and then into Eq. (43) yields the Ramsey formula:

$$P_1^R(\tau) = \frac{1}{2} \left[ 1 + e^{-\tau/T_2} \cos(\Delta\tau + \phi_0) \right]. \quad (44)$$

Eq. (44) shows that the fringe frequency is set by the detuning  $\Delta$ , and the contrast by  $T_2$ ;  $T_1$  does not enter explicitly because the  $\pi/2$  mapping eliminates  $Z(\tau)$ . In summary, Eqs. (32), (8), (10) together characterize energy relaxation and dephasing of the mechanically driven CNT, linking bath parameters to experimentally measurable Rabi- and Ramsey-decay envelopes.

#### S4. WIGNER FUNCTION FOR THE CNT COUPLED TO THE ENVIRONMENT

Immediately after preparation the CNT state is in the superposition  $|\psi(0)\rangle = \frac{|0\rangle + |1\rangle}{\sqrt{2}}$  with

$$\rho(0) = \frac{1}{2} \begin{pmatrix} 1 & 1 \\ 1 & 1 \end{pmatrix}$$



Coupling to a bath produces longitudinal relaxation at rate  $\Gamma_1 = 1/T_1$  and transverse decay at rate  $\Gamma_2 = 1/T_2$ . Within the Born–Markov approximation, and in the relaxation-limited regime (negligible pure dephasing, such that  $T_2 \simeq 2T_1$ ) and cold-bath limit ( $n_{\text{th}} \ll 1$ ), the density-matrix elements evolve as [21]:

$$\rho_{11}(t) = \rho_{11}(0) e^{-\Gamma_1 t}, \quad \rho_{00}(t) = 1 - \rho_{11}(t), \quad (45)$$

$$\rho_{01}(t) = \rho_{01}(0) e^{-t/T_2} e^{-i\omega_0 t} = \rho_{01}(0) e^{-(\Gamma_1/2)t} e^{-i\omega_0 t}, \quad \rho_{10}(t) = \rho_{01}^*(t). \quad (46)$$

The Wigner function for a state  $\rho = \sum_{m,n=0}^1 \rho_{mn} |m\rangle\langle n|$  is:

$$W(\alpha) = \frac{2}{\pi} e^{-2|\alpha|^2} \left[ \rho_{00} + \rho_{11} (4|\alpha|^2 - 1) + 2 \operatorname{Re}(2\alpha \rho_{10}) \right], \quad (47)$$

where  $\alpha = (X + iP)/\sqrt{2}$  is the phase-space coordinate. Writing  $\alpha = r e^{i\theta}$  with  $r \geq 0$ , and inserting Eq. (46) yields the time-dependent Wigner function:

$$W(r, \theta; t) = \frac{2}{\pi} e^{-2r^2} \left[ (1 - P(t)) + P(t) (4r^2 - 1) + 2r e^{-t/T_2} \cos(\theta - \omega_0 t) \right], \quad (48)$$

with  $P(t) = \rho_{11}(t) = \frac{1}{2} e^{-t/T_1}$ .

#### Limiting cases:

- *Initial state* ( $t = 0$ ):  $P(0) = \frac{1}{2} e^{-t/T_1} = 1$ ,

$$W(r, \theta; 0) = \frac{2}{\pi} e^{-2r^2} \left[ 2r^2 + 2r \cos \theta \right],$$

showing a negative lobe near the origin (quantum-interference signature).

- *Intermediate times*: the coherence term decays as  $e^{-t/T_2}$ , and the system is approaching a positive mixture of  $|0\rangle$  and  $|1\rangle$ .
- *Long times* ( $t \gg T_1$ ):  $P(t) \rightarrow 0$  and  $e^{-t/T_2} \rightarrow 0$ ,  $W \rightarrow \frac{2}{\pi} e^{-2r^2}$ , the Gaussian Wigner function of the ground state  $|0\rangle$ .

## S5. CALCULATION OF REPRESENTATIVE DEVICE PARAMETERS

*Geometry, material constants, and assumptions.* We model the suspended CNT as a uniform Euler–Bernoulli beam of length  $L$ , radius  $r$ , cross-section area  $A$  and moment of inertia  $I$ . Material parameters used throughout are Young’s modulus  $E = 1 \text{ TPa}$  and mass density  $\rho = 2200 \text{ kg/m}^3$ . For a thin-walled nanotube  $I/A \simeq r^2/2$ , yielding a fundamental flexural frequency [11]:

$$\omega_0 \simeq \frac{\beta_1^2 r}{\sqrt{2} L^2} \sqrt{\frac{E}{\rho}}. \quad (49)$$

with  $\beta_1 \approx 4.73$  for the fundamental mode. The linear frequency is  $f_0 = \omega_0/2\pi$  and scales as  $f_0 \propto L^{-2}$ .

*Effective mass and zero-point motion.* Let  $\phi_1(x)$  be the normalized fundamental mode shape and choose the readout/drive coordinate as the midspan displacement  $q(t) = w(x = L/2, t)$ . The associated effective mass is

$$m_{\text{eff}} = \mu \int_0^L \frac{\phi_1(x)^2}{\phi_1(L/2)^2} dx \equiv c_c \rho A L, \quad (50)$$

where  $c_c \simeq 0.735$  is a dimensionless geometric factor for the double-clamped beam [11].

The zero-point motion of this mode is then

$$x_{\text{zpf}} = \sqrt{\frac{\hbar}{2 m_{\text{eff}} \omega_0}} = \sqrt{\frac{\hbar}{2 c_c \rho A L \omega_0}} \propto L^{1/2}. \quad (51)$$

*Relaxation and coherence times, Rabi pulses and force scale.* The energy-relaxation time follows from the mechanical quality factor:

$$T_1 = \frac{Q}{\omega_0}, \quad T_2 \simeq 2T_1 \quad (\text{relaxation-limited, negligible pure dephasing}). \quad (52)$$

Because  $\omega_0 \propto L^{-2}$ , one has  $T_1 \propto L^2$  and  $T_2 \propto L^2$ .

A near-resonant AFM force  $F(t)$  couples as  $-F(t)x(t)$ . Within the rotating-wave approximation, the on-resonance Rabi rate obeys

$$\Omega_R(t) = \frac{F(t)x_{\text{zpf}}}{\hbar}, \quad \int \Omega_R(t) dt = \text{pulse area}. \quad (53)$$

A  $\pi/2$  pulse of duration  $t_{\pi/2}$  therefore requires

$$\Omega_R = \frac{\pi}{2t_{\pi/2}}, \quad F_{\pi/2} = \frac{\hbar \Omega_R}{x_{\text{zpf}}} = \frac{\pi \hbar}{2t_{\pi/2} x_{\text{zpf}}} \propto L^{-1/2}. \quad (54)$$

*Numerical evaluation of the parameters in Table I.* With the choices:

$$E = 1 \text{TPa}, \quad \rho = 2200 \text{ kg/m}^{-3}, \quad r = 1 \text{nm}, \quad c_c = 0.735, \quad Q = 10^4, \quad t_{\pi/2} = 100 \text{ ns},$$

we compute the entries of Table I for each  $L$ :

1.  $\omega_0$  from Eq. (49), then  $f_0 = \omega_0/2\pi$ .
2.  $m_{\text{eff}} = c_c \rho A L$  via Eq. (50).
3.  $x_{\text{zpf}}$  from Eq. (51).
4.  $F_{\pi/2}$  from Eq. (54).
5.  $T_1 = Q/\omega_0$  and  $T_2 \simeq 2T_1$  from Eq. (52).